# Olivine-Type Nanosheets for Lithium Ion Battery Cathodes

**Xianhong Rui,[†] Xiaoxu Zhao,[†] Ziyang Lu,[†] Huiteng Tan,[†] Daohao Sim,[†] Huey Hoon Hng,[†] Rachid Yazami,[†] Tuti Mariana Lim,[‡] and Qingyu Yan[†,§,⊥,*]**

[†]School of Materials Science and Engineering and [‡]School of Civil and Environmental Engineering, Nanyang Technological University, 639798, Singapore and [§]Energy Research Institute and [⊥]TUM CREATE Centre for Electromobility, Nanyang Technological University, 637459, Singapore

**ABSTRACT** Olivine-type $LiMPO_4$ (M = Fe, Mn, Co, Ni) has become of great interest as cathodes for next-generation high-power lithium-ion batteries. Nevertheless, this family of compounds suffers from poor electronic conductivities and sluggish lithium diffusion in the [010] direction. Here, we develop a liquid-phase exfoliation approach combined with a solvothermal lithiation process in high-pressure high-temperature (HPHT) supercritical fluids for the fabrication of ultrathin $LiMPO_4$ nanosheets (thickness: 3.7−4.6 nm) with exposed (010) surface facets. Importantly, the HPHT solvothermal lithiation could produce monodisperse nanosheets while the traditional high-temperature calcination, which is necessary for cathode materials based on high-quality crystals, leads the formation of large grains and aggregation of the nanosheets. The as-synthesized nanosheets have features of high contact area with the electrolyte and fast lithium transport (time diffusion constant in at the microsecond level). The estimated diffusion time for $Li^+$ to diffuse over a [010]-thickness of <5 nm ($L$) was calculated to be less than 25, 2.5, and 250 $\mu$s for $LiFePO_4$, $LiMnPO_4$, and $LiCoPO_4$ nanosheets, respectively, *via* the equation of $t = L^2/D$. These values are about 5 orders of magnitude lower than the corresponding bulk materials. This results in high energy densities and excellent rate capabilities (*e.g.*, 18 kW $kg^{-1}$ and 90 Wh $kg^{-1}$ at a 80 C rate for $LiFePO_4$ nanosheets).

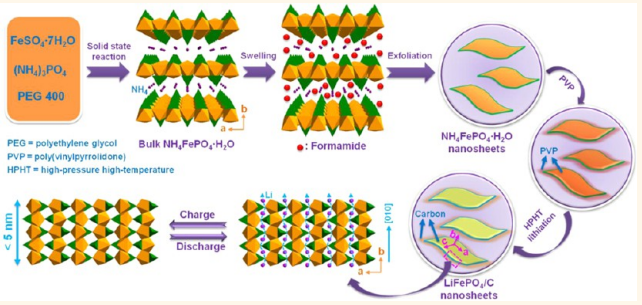


**KEYWORDS:** ultrathin nanosheets · supercritical fluids · olivine · cathodes · lithium-ion batteries

Nanosheets, which possess thicknesses on the order of nanometers and lateral dimensions of submicro- to micrometers, are currently regarded as a new class of two-dimensional (2D) materials owing to their exotic electronic properties and high specific surface areas compared with the corresponding bulk materials. They are considered to be important for many applications in areas ranging from photocatalysis to electrodes of electrochemical devices.[1−6] Since great progress has been made in the graphene area,[1,7−10] a wide variety of free-floating 2D nanosheets, including metals,[3] oxides,[4,11−13] hydroxides,[14] and chalcogenides,[15−17] have been synthesized. However, it still remains a great challenge to grow 2D nanosheets with more sophisticated compositions, such as "polyanion" compounds.

Olivine-type lithium transition-metal phosphates $LiMPO_4$ (M = Fe, Mn, Co, or Ni) have attracted great interest as cathodes for rechargeable lithium ion batteries (LIBs) owing to their high energy density, thermal stability, environmental friendliness, and low raw materials cost.[18−23] Despite these favorable properties, the rate capabilities of all the $LiMPO_4$ materials are highly restricted by the sluggish kinetics of electron and lithium-ion transport.[24−26] Strategies to increase the rate performance of $LiMPO_4$ have focused on improving electron transport in the bulk (aliovalent doping[18,20,27−29]) or at the surface of the material (coating with a conductive layer, *e.g.*, carbon,[30−32] conductive polymers,[33] Ag,[34] and $RuO_2$[35]), or on reducing the diffusion distance for both Li ions and electrons by fabricating nanosized materials (*e.g.*, nanoparticles,[31] nanowires,[36] and hollow structured nanospheres[37]). However, recent evidence shown by atomistic simulations[28] and experiments[38] indicate that Li ions can only move along the [010] or *b*-axis direction in the orthorhombic $LiMPO_4$ crystals. Therefore, ultrathin 2D $LiMPO_4$ nanosheets with exposed (010) surface facets are highly desired for fast lithium diffusion to

* Address correspondence to alexyan@ntu.edu.sg.

Received for review May 3, 2013 and accepted May 28, 2013.

**Published online May 28, 2013**
10.1021/nn4022263

achieve high-rate capability. Herein, we report an effective and easily scaled-up synthetic procedure for the preparation of ultrathin carbon-coated $LiMPO_4$ ($LiMPO_4$/C) nanosheets with a thickness of 3.8–4.6 nm. The synthesis is based on a liquid-phase exfoliation approach combined with a solvothermal lithiation process in high-pressure high-temperature (HPHT) supercritical fluids. The traditional high-temperature solid-state lithiation causes a serious aggregation and coarsening of the nanostructures. The as-synthesized $LiMPO_4$/C nanosheets have a large specific surface area (108–143 $m^2\ g^{-1}$), and short lithium diffusion paths, which result in electrodes having high energy densities and excellent rate capabilities (*e.g.*, 18 kW $kg^{-1}$ and 90 Wh $kg^{-1}$ at a 80 C rate for $LiFePO_4$/C nanosheets).

## RESULTS AND DISCUSSION

The $LiFePO_4$/C nanosheet was employed as a representative case for studying the growth of $LiMPO_4$/C nanosheets, and its synthetic strategy is schematically depicted in Figure 1. First, layered bulk ammonium iron phosphate $NH_4FePO_4 \cdot H_2O$ (Figure S1, Supporting Information) was prepared according to previously reported solid state methods.[39] Subsequently, bulk $NH_4FePO_4 \cdot H_2O$ was swelled by intercalation of formamide molecules into the interlayer space (Figure S2, Supporting Information), resulting in significantly weakened interlayer attraction. Mechanical shaking (*i.e.*, ultrasonication) was then introduced to impose a transverse sliding force on the swollen phase, leading to the exfoliation of the $NH_4FePO_4 \cdot H_2O$ layers. Afterward, the resulting $NH_4FePO_4 \cdot H_2O$ nanosheets were immersed into an ethanol solution containing poly(vinylpyrrolidone) (PVP). Within this step, the surfactant PVP with amphiphilic characteristics was expected to adsorb on the surface of $NH_4FePO_4 \cdot H_2O$ nanosheets (Figure S3, Supporting Information). Finally, the HPHT (10 MPa, 400 °C) solvothermal lithiation converted PVP-capped $NH_4FePO_4 \cdot H_2O$ nanosheets into $LiFePO_4$/C nanosheets. During this process, PVP can not only prevent the agglomerations of nanosheets, but also be transformed into conductive amorphous carbon layer coated on $LiFePO_4$ nanosheet surfaces.

The X-ray diffraction (XRD) pattern for the exfoliated $NH_4FePO_4 \cdot H_2O$ nanosheet precursor (Figure 2A) shows the sole strong diffraction peak from the (010) planes of orthorhombic $NH_4FePO_4 \cdot H_2O$ phase (JCPDS No. 45-0424), which indicates the highly preferred (010) orientation. The transmission electron microscopy (TEM) image of the exfoliated product (Figure 2B) exhibits a 2D thin sheet structure with lateral dimensions of about 500 nm. The well-defined Tyndall effect of a transparent solution of $NH_4FePO_4 \cdot H_2O$ nanosheets (Figure 2C) indicates the presence of highly monodisperse ultrathin nanosheets in formamide. The atomic force microscopy (AFM) analysis reveals that the thickness of the as-obtained $NH_4FePO_4 \cdot H_2O$ nanosheets is about 1.9 nm (Figure S4, Supporting Information). The selected area electron diffraction (SAED) pattern in

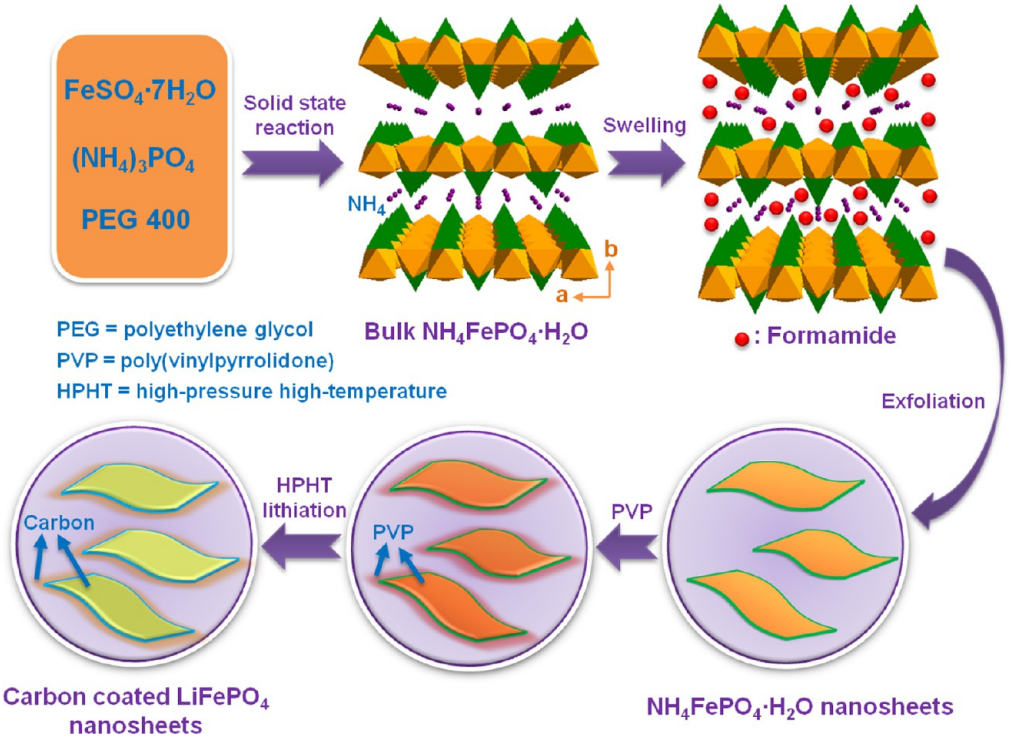


**Figure 1. Schematic illustration of the preparation of carbon-coated $LiFePO_4$ nanosheets through a liquid-phase exfoliation approach combined with a HPHT solvothermal lithiation process.**

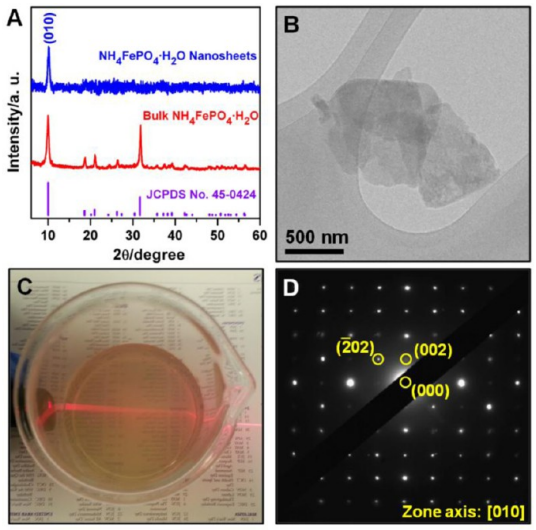


**Figure 2. Characterizations of exfoliated $NH_4FePO_4 \cdot H_2O$ nanosheet precursor. (A) XRD patterns of (010)-oriented freestanding $NH_4FePO_4 \cdot H_2O$ nanosheets, bulk $NH_4FePO_4 \cdot H_2O$, and JCPDS standard card. (B) TEM image. (C) The red laser beam emitted from the left side to demonstrate Tyndall effect of the $NH_4FePO_4 \cdot H_2O$ nanosheet in formamide solution. (D) SAED pattern.**

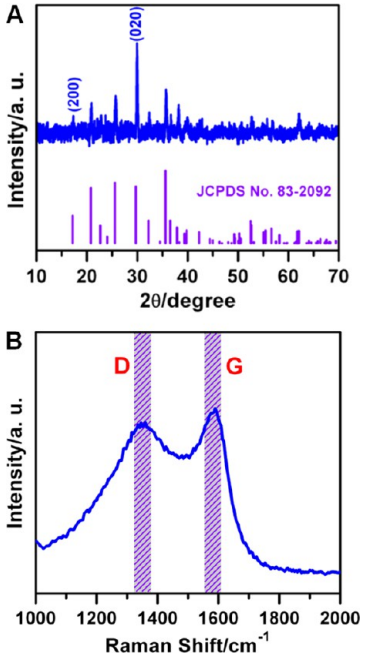


**Figure 3. (A) XRD pattern and (B) Raman spectrum of the as-prepared $LiFePO_4$/C nanosheets.**

Figure 2D reveals that the $NH_4FePO_4 \cdot H_2O$ nanosheet is a single crystal with the [010] zone axis projection, further confirming the (010) orientation in accordance with the XRD analysis.

The as-prepared $NH_4FePO_4 \cdot H_2O$ nanosheets capped by PVP molecules were then transformed into $LiFePO_4$/C nanosheets by a HPHT solvothermal lithiation process. In comparison, the sample fabricated *via* conventional high-temperature solid-state reaction of $NH_4FePO_4 \cdot H_2O$ nanosheets with stoichiometric $CH_3COOLi \cdot H_2O$ in Ar atmosphere at 700 °C for 10 h is seriously agglomerated (Figure S5, Supporting Information). The crystallographic structure of the final nanosheet product was examined by XRD (Figure 3A). All the diffraction peaks can be indexed as the orthorhombic $LiFePO_4$ phase (JCPDS No. 83-2092). No impurity peaks are detected. Interestingly, the intensity ratio of $I_{(020)}/I_{(200)} = 5.6$ is much larger than that of the standard card ($I_{(020)}/I_{(200)} = 2.1$), implying a 2D structure with preferential direction along the *ac* plane.[40] The nature of the carbon coating on $LiFePO_4$ surface was studied using Raman spectroscopy (Figure 3B). Two characteristic bands of carbonaceous materials were detected at around 1350 $cm^{-1}$ (D-band, disorder-induced phonon mode) and at ~1590 $cm^{-1}$ (G-band, graphite band), which agree well with amorphous carbon.[41] The optical micrograph (Figure S6, Supporting Information) and TEM observation (Figure 4A) confirm the formation of a large number of 2D nanosheets with lateral dimensions of ~500 nm. Similarly, clear Tyndall light scattering was also discerned for the $LiFePO_4$/C nanosheet suspension (Figure 4B), reasonably indicating the formation of abundant freestanding and homogeneous 2D ultrathin sheets. The high resolution (HR) TEM image taken from the center of the nanosheet shows two sets of lattices with interfringe spacings of 0.43 and 0.19 nm (Figure 4C), corresponding to the *d*-spacings of the (101) and (501) planes of orthorhombic $LiFePO_4$ (JCPDS No. 83-2092), respectively. In addition, an amorphous carbon layer with a thickness of 0.5−1.1 nm covers the surface of the $LiFePO_4$ nanosheet (Figure 4D). The spotted SAED pattern shown in Figure 4E reveals the single-crystalline nature of the $LiFePO_4$ nanosheet, and can be indexed to the [010] zone axis, indicating that the $LiFePO_4$ nanosheet shows major exposure of (010) facets. AFM analysis demonstrates that the thickness of a $LiFePO_4$/C nanosheet is ~4.3 nm (Figure 4F). The specific surface area of $LiFePO_4$/C nanosheets was measured by nitrogen adsorption/desorption isotherms (Figure S7, Supporting Information) and was estimated to be as high as 128.5 $m^2\ g^{-1}$ using the Brunauer−Emmett−Teller (BET) method.

On the basis of the crystal structure similarity, the above synthetic strategy has been extended to prepare ultrathin $LiMnPO_4$/C, $LiCoPO_4$/C, and $LiNiPO_4$/C nanosheets. First, $NH_4MnPO_4 \cdot H_2O$, $NH_4CoPO_4 \cdot H_2O$, and $NH_4NiPO_4 \cdot H_2O$ nanosheet precursors were successfully fabricated by liquid-exfoliation of their bulk counterparts (Figure S8, Supporting Information) in formamide solution. In the experimental XRD patterns of the exfoliated nanosheet precursors (Figure 5A−C), compared with those of corresponding standard phases and bulk materials, only the lattice planes with integer multiple indexes of (010) are detected, implying that these nanosheets have well-defined

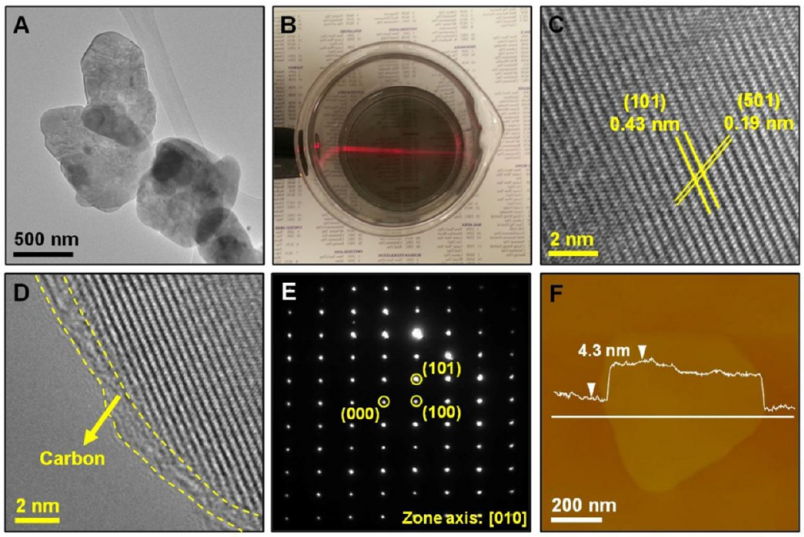


**Figure 4. Characterizations of $LiFePO_4$/C nanosheets. (A) TEM image and (B) corresponding colloidal ethanol suspension displaying the Tyndall effect. (C and D) HRTEM images. (E) SAED pattern revealing the exposure of (010) facets. (F) AFM image and corresponding height profile.**

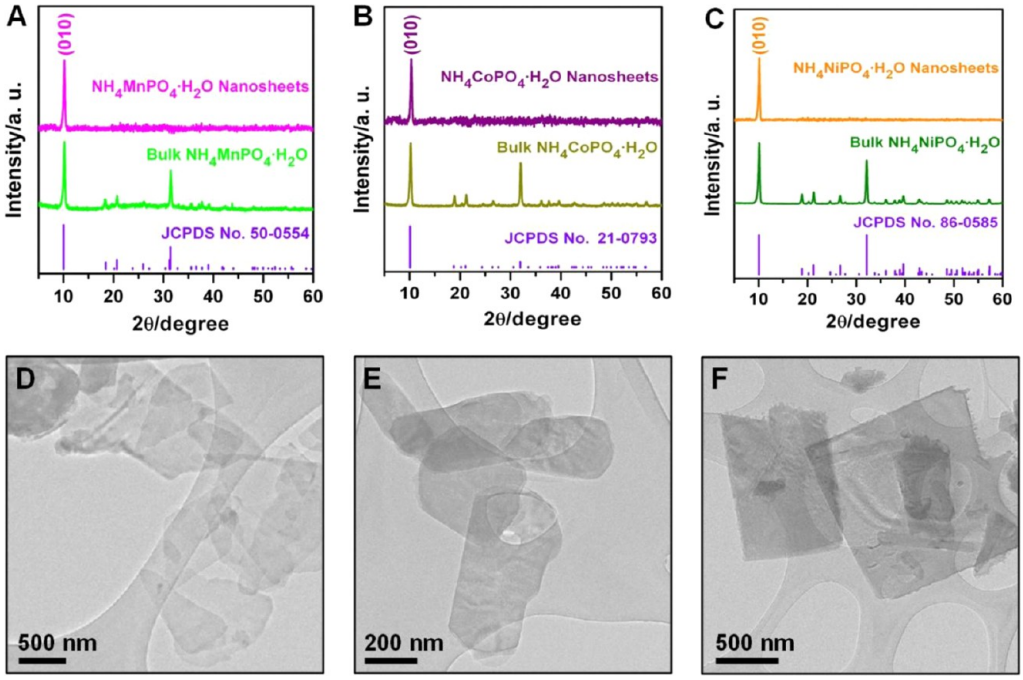


**Figure 5. (A–C) XRD patterns, and (D–F) TEM images of $NH_4MnPO_4·H_2O$ (A, D), $NH_4CoPO_4·H_2O$ (B, E), and $NH_4NiPO_4·H_2O$ (C, F) nanosheet precursors.**

(010) crystal plane orientations, which are further verified by the corresponding SAED patterns (zone axis: [010], Figure S9, Supporting Information). TEM images in Figure 5D–F present free-standing ultrathin $NH_4MnPO_4·H_2O$, $NH_4CoPO_4·H_2O$, and $NH_4NiPO_4·H_2O$ nanosheets with lateral dimensions of 0.5–1.5, ~0.5, and 0.5–1.0 $\mu$m, respectively. AFM analyses (Figure S10, Supporting Information) reveal that the as-obtained $NH_4MnPO_4·H_2O$, $NH_4CoPO_4·H_2O$, and $NH_4NiPO_4·H_2O$ nanosheets have thicknesses of around 1.6, 2.1, and 1.7 nm, respectively. Subsequent HPHT (10 MPa, 400 °C) solvothermal lithiation of PVP-capped $NH_4MnPO_4·H_2O$, $NH_4CoPO_4·H_2O$, and $NH_4NiPO_4·H_2O$ nanosheets led to the formation of $LiMnPO_4$/C, $LiCoPO_4$/C, and $LiNiPO_4$/C nanosheets, respectively, and their crystal structures were investigated by XRD technology. All of the reflections in Figure 6A–C can be indexed as an orthorhombic olivine structure of $LiMnPO_4$ (JCPDS No. 74-0375), $LiCoPO_4$ (JCPDS No. 32-0552), and $LiNiPO_4$ (JCPDS No. 88-1297) with a space group of *Pnma*. The extremely high $I_{(020)}/I_{(200)}$ ratios ($LiMnPO_4$, 7.7; $LiCoPO_4$, 3.7; and

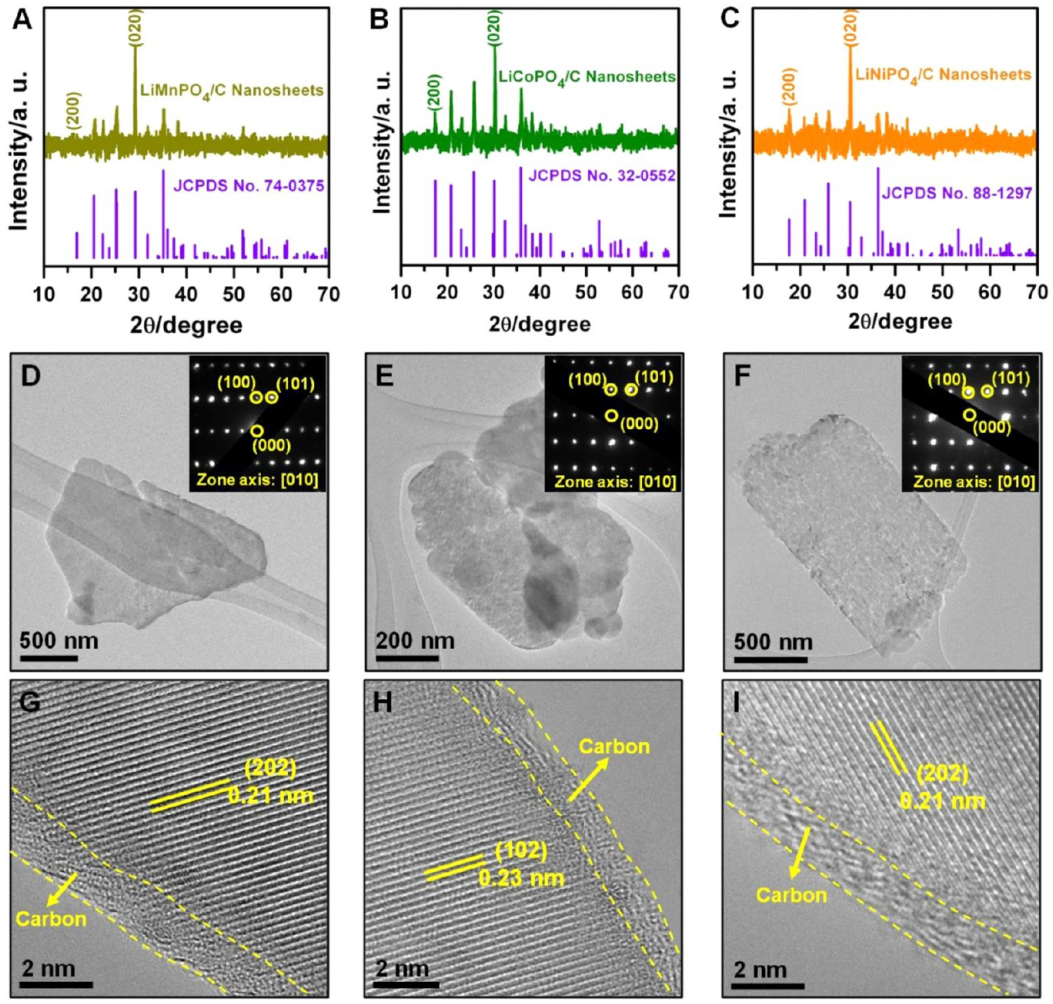


**Figure 6. (A–C) XRD patterns, (D–F) TEM images, and (G–I) HRTEM images of $LiMnPO_4$/C (A, D, G), $LiCoPO_4$/C (B, E, H), and $LiNiPO_4$/C (C, F, I) nanosheets. Insets in panels D–F: corresponding SAED patterns with zone axis of [010].**

$LiNiPO_4$, 3.5) as compared with those of the standard cards ($LiMnPO_4$, 2.6; $LiCoPO_4$, 1.0; and $LiNiPO_4$, 1.4) indicate the preferred *ac*-plane orientation. In addition, the formation of the amorphous carbon coating layer was confirmed by the Raman spectra (Figure S11, Supporting Information) with characteristic D-band (~1350 $cm^{-1}$) and G-band (~1590 $cm^{-1}$). TEM images (Figure 6D–F) reveal that the final lithiated products retain the nanosheet morphology. The SAED patterns (insets in Figure 6D–F) taken from individual nanosheets exhibit the single-crystalline properties and can be identified as the [010] projection of the orthorhombic olivine-type reciprocal lattices, implying an exposure of (010) facets. The interlayer spacings in the HRTEM images in Figure 6G–I are measured to be 0.21, 0.23, and 0.21 nm, respectively, agreeing well with the *d*-spacings of the (202) planes of $LiMnPO_4$, (102) planes of $LiCoPO_4$, and (202) planes of $LiNiPO_4$. Additionally, it also can be seen from Figure 6G–I that a thin carbon layer (approximately 0.5–1.5 nm thick) covers the surface of the $LiMnPO_4$, $LiCoPO_4$, and $LiNiPO_4$ nanosheets. These $LiMnPO_4$/C, $LiCoPO_4$/C, and $LiNiPO_4$/C nanosheets possess the AFM thicknesses of about 3.7, 4.6, and 4.0 nm (Figure S12, Supporting Information), respectively. The measured BET surface area for $LiMnPO_4$/C, $LiCoPO_4$/C, and $LiNiPO_4$/C nanosheets is 142.9, 107.6, and 136.4 $m^2\ g^{-1}$ (Figure S13, Supporting Information), respectively. These values combined with that of $LiFePO_4$/C (128.5 $m^2\ g^{-1}$) are well consistent with the calculated specific surface areas (about 140 $m^2\ g^{-1}$) for ~4 nm-thick $LiMPO_4$/C sheets on the basis of skeletal densities of these sheets ($LiMPO_4$ + ~5 wt % C, ~3.5 g $cm^{-3}$), further indicating the homogeneity of monodispersed nanosheets. The above results clearly demonstrate that the strategy shown in Figure 1 is a general approach and is highly effective in yielding ultrathin olivine-type carbon-coated $LiMPO_4$ nanosheet electroactive materials.

Motivated by the unique inherent structure of ultrathin $LiMPO_4$/C nanosheets, a series of electrochemical Li storage measurements were carried out based on the Li half cell configuration. Here, it is worth mentioning that $LiNiPO_4$ has very high Li extraction potential (around 5.3 V),[42] suffering the problem of serious

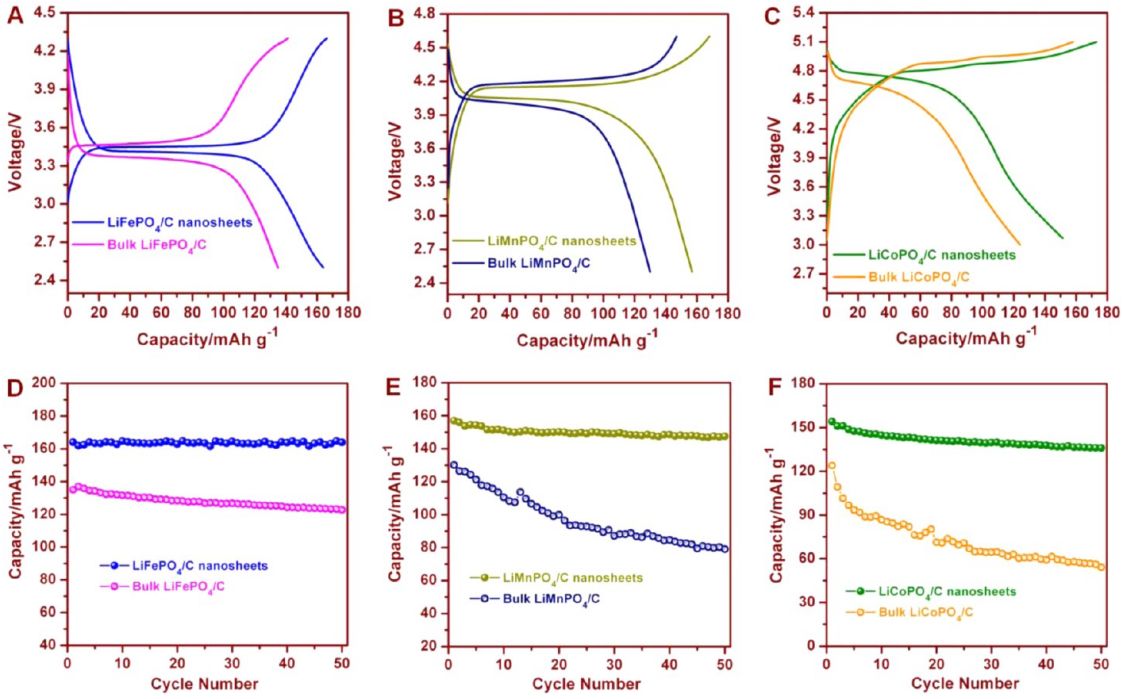


**Figure 7. (A–C) The initial galvanostatic charge–discharge voltage profiles, and (D–F) cycling performances of $LiFePO_4$/C (A, D), $LiMnPO_4$/C (B, E), and $LiCoPO_4$/C (C, F) at a rate of 0.2 C.**

electrolyte oxidation. Therefore, we did not evaluate its electrochemical Li storage properties. The initial galvanostatic charge–discharge voltage profiles (Figure 7A–C) of $LiFePO_4$/C, $LiMnPO_4$/C, and $LiCoPO_4$/C nanosheets were tested at a rate of 0.2 C (1 C = 170 mA $g^{-1}$). The cells exhibit the typical voltage plateaus along 3.4, 4.1, and 4.8 V for $LiFePO_4$/C, $LiMnPO_4$/C, and $LiCoPO_4$/C nanosheets, respectively, corresponding to the $Li^+$ extraction/insertion processes *via* the reaction of $LiMPO_4$ (M = Fe, Mn, Co) $- Li^+ - e^- \leftrightarrow MPO_4$.[43] These electrochemical activities yield initial discharge capacities of 164, 157, and 153 mAh $g^{-1}$ with Coulombic efficiency of 98%, 93%, and 88% for $LiFePO_4$/C, $LiMnPO_4$/C, and $LiCoPO_4$/C nanosheets, respectively. Moreover, these nanosheets exhibit good cycling stabilities (Figure 7D–F). During the 50th cycle under a rate of 0.2 C, $LiFePO_4$/C, $LiMnPO_4$/C, and $LiCoPO_4$/C nanosheets still retain reversible discharge capacities of 163, 147, and 136 mAh $g^{-1}$, corresponding to 99.4%, 93.6%, and 88.3% of their initial discharge capacities, respectively. Additionally, the straightforward and flat voltage plateaus with almost no variation can still be observed during the 50th cycle (Figure S14A–C, Supporting Information), indicating the highly reversible phase transition processes. For comparison, we also prepared bulk $LiFePO_4$/C, $LiMnPO_4$/C, and $LiCoPO_4$/C without the liquid-phase exfoliation procedure while we kept other experimental parameters the same (see chemical physical characterizations, Figure S15–17, Supporting Information). In contrast, the bulk $LiFePO_4$/C, $LiMnPO_4$/C, and $LiCoPO_4$/C show large polarizations in their charge/discharge voltage profiles and deliver much lower initial discharge capacities of 134, 130, and 124 mAh $g^{-1}$ (Figure 7A–C), respectively. The difference is mainly related to the much longer diffusion distance for the Li ion and electron transportation in the bulk counterparts. The bulk materials also suffer from an abrupt capacity fading, with a capacity retention of only 91.1%, 60.8%, and 43.5% during the 50th cycle for $LiFePO_4$/C, $LiMnPO_4$/C, and $LiCoPO_4$/C electrodes, respectively (Figure 7D–F). Moreover, the discharge polarizations of bulk electrodes become more pronounced with prolonged lithium uptake and removal as revealed by the obscure and decreased discharge voltage plateaus during the 50th cycle (Figure S14D–F, Supporting Information).

The remarkable advantage of ultrathin $LiMPO_4$/C nanosheets is their excellent rate capability, which is highly desirable for high-power LIB applications such as hybrid electric vehicles (HEVs) and electric vehicles (EVs). The cycling responses of these nanosheets at different C rates (each sustained for five cycles) were evaluated and shown in Figure 8A–C. Stable cycling performances were obtained for all rates. As Figure 8A shows, the discharge capacities of $LiFePO_4$/C nanosheet electrode are 139, 121, and 100 mAh $g^{-1}$ at discharge rates of 10, 20, and 50 C, respectively. Even at an ultrahigh rate of 80 C, it still delivers a discharge capacity of 70 mAh $g^{-1}$ (corresponding to a 45 s total discharge time), thereby indicating its excellent high-power performance. $LiMnPO_4$/C nanosheets present a discharge capacity of 119 mAh $g^{-1}$ at 5 C, and decrease to 95, 63, and 40 mAh $g^{-1}$ as the discharge rate increases to 10, 20, and 30 C, respectively (Figure 8B).

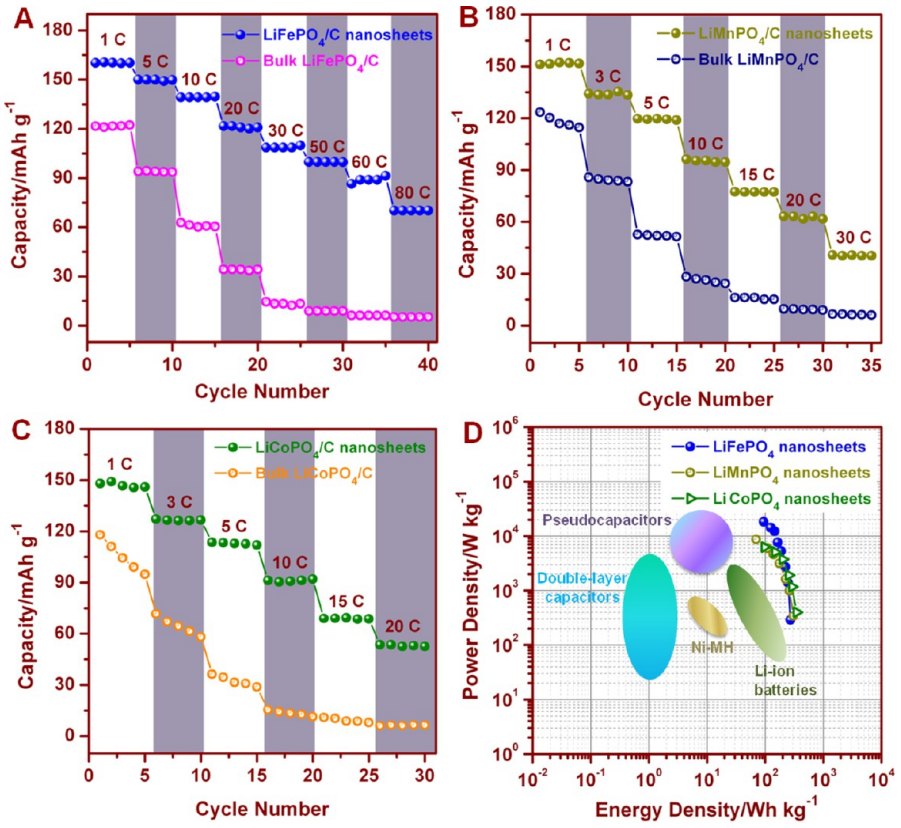


**Figure 8. Rate capabilities of $LiFePO_4$/C (A), $LiMnPO_4$/C (B), and $LiCoPO_4$/C (C). (D) The Ragone plot of $LiMPO_4$/C nanosheets, in comparison with some advanced energy storage and conversion devices.**

At the rates of 5, 10, and 20 C, the discharge capacities of $LiCoPO_4$/C nanosheets are 113, 91, and 53 mAh $g^{-1}$, respectively (Figure 8C). These C-rate properties are significantly better than corresponding bulk counterparts with almost no electrochemical responses at rates from 10 to 30 C (Figure 8A–C), which is mainly attributed to poor charge transfer kinetics of the bulk electrodes as verified by the electrochemical impedance spectra (Figure S18, Supporting Information). The bulk electrodes show larger radii of semicircles in the Nyquist plots than those of the corresponding nanosheet electrodes, and thus indicate higher charge-transfer resistance and more sluggish kinetics of the Faradic reactions. On the other hand, the rate capabilities of $LiMnPO_4$/C and $LiCoPO_4$/C nanosheets are slightly poorer as compared with the $LiFePO_4$ nanosheets, which may be ascribed to the difference in intrinsic material properties, such as the electrical conductivity.

Our work provides evidence that extremely high electrochemical discharge rates can be achieved with $LiMPO_4$/C nanosheets. Their power and energy performances were further evaluated with a Ragone plot, which were calculated based on the weight of both positive and negative electrodes, working voltages, and the capacities at various rates, and compared with some advanced energy storage and conversion devices (Figure 8D).[44−49] At a low specific power of <1 kW $kg^{-1}$, $LiMPO_4$/C nanosheets exhibit gravimetric energies as high as 250−350 Wh $kg^{-1}$, indicating high energy-storage performances. With increased specific power of 5−10 kW $kg^{-1}$, the cells still possess gravimetric energies of 100−180 Wh $kg^{-1}$, indicating high-power capabilities. In the case of $LiFePO_4$/C nanosheets, an ultrahigh power density of 18 kW $kg^{-1}$ (energy density: 90 Wh $kg^{-1}$) can still be realized. Such cells could provide much higher power densities than current nickel metal−hydride (100−1000 W $kg^{-1}$) and lithium-ion battery (800−2000 W $kg^{-1}$), while the energy densities are several times greater than that of supercapacitor technology (1−20 Wh $kg^{-1}$).[45] These capabilities indicate that $LiMPO_4$/C nanosheets, especially for $LiFePO_4$/C, can be used to build superior energy storage and conversion devices (*e.g.*, HEVs, and EVs) with both high-power and high-energy densities.

Plausible mechanisms resulting in the observed excellent rate performances of $LiMPO_4$/C nanosheets are proposed as shown in the scheme (Figure 9). (1) Ultrathin nanosheets with large surface area (108−143 $m^2$ $g^{-1}$) permit high contact area with the electrolyte and hence high $Li^+$ flux across the interface.[50−52] (2) $Li^+$ transport processes are ultrafast. According to the estimated values of the lithium diffusion coefficients ($D$) of $LiMPO_4$ ($LiFePO_4$, ~$10^{-8}$ $cm^2$ $s^{-1}$; $LiMnPO_4$, ~$10^{-7}$ $cm^2$ $s^{-1}$; and $LiCoPO_4$, ~$10^{-9}$ $cm^2$ $s^{-1}$)[53] in the [010] direction, the time ($t$) for $Li^+$ to diffuse over

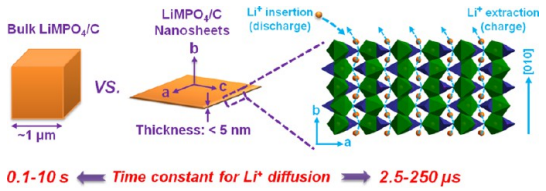


**Figure 9. A schematic of lithiation/delithiation processes for bulk $LiMPO_4$/C versus (010)-oriented ultrathin $LiMPO_4$/C nanosheets. Ultrafast lithium storage is observed for ultrathin $LiMPO_4$/C nanosheets.**

a [010]-thickness of <5 nm (*L*) was calculated to be less than 25, 2.5, and 250 $\mu$s for $LiFePO_4$/C, $LiMnPO_4$/C, and $LiCoPO_4$/C nanosheets, respectively, *via* the equation of $t = L^2/D$. These values are about 5 orders of magnitude lower than the corresponding bulk materials.

## CONCLUSIONS

We have demonstrated that olivine-type (010)-oriented $LiMPO_4$ nanosheets with thicknesses of only 3.7−4.6 nm were prepared through a liquid-phase exfoliation combined with subsequent solvothermal lithiation process in HPHT supercritical fluids. These nanosheets are single crystalline with large specific surface area (108−143 $m^2\ g^{-1}$). The unique ultrathin nanosheet features (*e.g.*, ultrafast lithium transport) result in electrodes having high energy densities and excellent rate capabilities (*e.g.*, 18 kW $kg^{-1}$ and 90 Wh $kg^{-1}$ at a 80 C rate for $LiFePO_4$/C nanosheets), which will blur the distinction between supercapacitors and batteries, opening up prospects for HEV and EV applications.

## METHODS

**Synthesis of $NH_4MPO_4 \cdot H_2O$ Nanosheets.** All the starting materials were of analytically pure grade and used as received. Bulk $NH_4MPO_4 \cdot H_2O$ was prepared according to previously reported solid state methods.[39] First, $(NH_4)_3PO_4 \cdot 3H_2O$ was ground with $FeSO_4 \cdot 7H_2O$, $MnSO_4 \cdot H_2O$, $CoSO_4 \cdot 7H_2O$, and $NiSO_4 \cdot 6H_2O$, respectively, with a molar ratio of 1:1 for 30 min. Following, the mixture was ground for another 60 min after addition of nonionic surfactant polyethylene glycol (PEG) 400 and then put into a vacuum oven at 40 °C for 48 h. The bulk $NH_4MPO_4 \cdot H_2O$ crystals were collected and washed with deionized water and ethanol solution for several times and dried in a vacuum oven at 80 °C for 12 h. Afterward, the as-obtained bulk $NH_4MPO_4 \cdot H_2O$ powder (50 mg) was added into a 100 mL glass bottle containing a formamide solution (50 mL), and the whole mixture was shaken to suspend the powder and kept overnight. The resulting suspension was then sonicated at room temperature for about 3 days. After ultrasonic treatment, the exfoliated $NH_4MPO_4 \cdot H_2O$ nanosheets were isolated from the upper solution of glass bottle *via* centrifugation, washed with ethanol for several times to remove residual formamide, and then dried in a vacuum oven (80 °C) for overnight.

**Synthesis of $LiMPO_4$/Carbon Nanosheets.** In a typical procedure, the as-synthesized $NH_4MPO_4 \cdot H_2O$ nanosheets (20 mg) were dispersed in an ethanol solution (50 mL) containing surfactant PVP (50 mg) under magnetic stirring. After 1 h, the surface of the $NH_4MPO_4 \cdot H_2O$ nanosheets are completely capped with molecular PVP. The suspension was then centrifuged and redispersed in an ethanol solution (30 mL). Subsequently, stoichiometric $CH_3COOLi \cdot H_2O$ was added. After that, the above solution was put into a high-pressure high-temperature reactor and maintained at 10 MPa and 400 °C for 2 h. Finally, the $LiMPO_4$/carbon nanosheets were collected and washed with deionized water and ethanol solution, and dried in a vacuum oven (80 °C) for 12 h. The carbon content was determined to be around 4.6, 5.2, 4.4, and 4.9 wt % for $LiFePO_4$/C, $LiMnPO_4$/C, $LiCoPO_4$/C, and $LiNiPO_4$/C nanosheets, respectively, *via* a previously reported method[54] by dissolving $LiMPO_4$/C nanosheets in a hydrochloric acid solution and weighing the remains. In comparison, bulk $LiMPO_4$/C was also prepared without the liquid-exfoliation procedure while other experimental parameters were kept same. The carbon content was around 2.0, 2.5, 1.5, and 2.5 wt % for bulk $LiFePO_4$/C, $LiMnPO_4$/C, $LiCoPO_4$/C, and $LiNiPO_4$/C, respectively.

**Materials Characterization.** X-ray powder diffraction (XRD) patterns were recorded on a Bruker AXS D8 Advance X-ray diffractometer using Cu K$\alpha$ radiation. The morphology was investigated by using a field-emission scanning electron microscopy (FESEM) system (JEOL, model JSM-7600F), and the nanostructure was characterized by using a transmission electron microscopy (TEM) instrument (JEOL, model JEM-2010 and 2100F) operating at 200 kV. FT-IR spectra were recorded on a Fourier transform infrared spectrometer (Perkin-Elmer) with a DGTS detector. Raman spectra were acquired by a WITec CRM200 confocal Raman microscopy system with a laser wavelength of 488 nm and a spot size of 0.5 mm. Nitrogen adsorption/desorption isotherms were conducted at 77 K (ASAP 2020). Atomic force microscopy (AFM) (Digital Instruments) was used to determine the thicknesses of $NH_4MPO_4 \cdot H_2O$ and $LiMPO_4$/C nanosheets.

**Electrochemical Measurements.** The coin-type cells were assembled in an argon-filled glovebox, where both moisture and oxygen levels were less than 1 ppm. The electrodes were fabricated by mixing of 80 wt % $LiMPO_4$/C nanosheets or bulk $LiMPO_4$/C with multiwalled carbon nanotube (10 wt %) and polyvinylidene fluoride (PVDF, 10 wt %) in *n*-methyl-2-pyrrolidone (NMP) solvent, and then pasted onto the aluminum foils (Ø = 14 mm). The mass loading was around 2.0 mg. Lithium foils were used as anodes and the electrolyte solution was made of 1 M $LiPF_6$ in ethylene carbonate (EC)/diethyl carbonate (DEC) (1/1, w/w). The cells were tested on a NEWARE multichannel battery test system with galvanostatic charge and discharge in the voltage ranges of 2.5−4.3 V ($LiFePO_4$/C), 2.5−4.6 V ($LiMnPO_4$/C), and 3.0−5.1 V ($LiCoPO_4$/C). The specific capacity values in this paper were on the basis of pure $LiMPO_4$. Electrochemical impedance spectra (frequency range: 0.001−$10^5$ Hz) of electrodes in coin-type cells were performed with an electrochemical workstation (CHI 660C).

*Conflict of Interest:* The authors declare no competing financial interest.

*Supporting Information Available:* Chemical physical characterizations (XRD patterns, SEM images, Raman spectra, and nitrogen adsorption/desorption isotherms) for bulk $NH_4MPO_4 \cdot H_2O$ and bulk $LiMPO_4$/C, and additional information (XRD patterns, FTIR spectra, AFM images, optical micrograph, SAED patterns, Raman spectra, and nitrogen adsorption/desorption isotherms) for $NH_4MPO_4 \cdot H_2O$ nanosheet precursors and final $LiMPO_4$/C nanosheets. Charge−discharge voltage profiles and electrochemical impedance spectra. This material is available free of charge *via* the Internet at http://pubs.acs.org.

*Acknowledgment.* The authors gratefully acknowledge, NRF2009EWT-CERP001-026 (Singapore), A*STAR SERC Grant 1021700144 and a Singapore MPA 23/04.15.03 grant, and Singapore National Research Foundation under CREATE program: EMobility in Megacities.

## REFERENCES AND NOTES

1. Geim, A. K. Graphene Status and Prospects. *Science* **2009**, *324*, 1530–1534.

2. Tang, Z. Y.; Zhang, Z. L.; Wang, Y.; Glotzer, S. C.; Kotov, N. A. Self-Assembly of CdTe Nanocrystals into Free-Floating Sheets. *Science* **2006**, *314*, 274–278.
3. Huang, X. Q.; Tang, S. H.; Mu, X. L.; Dai, Y.; Chen, G. X.; Zhou, Z. Y.; Ruan, F. X.; Yang, Z. L.; Zheng, N. F. Freestanding Palladium Nanosheets with Plasmonic and Catalytic Properties. *Nat. Nanotechnol.* **2011**, *6*, 28–32.
4. Rui, X. H.; Lu, Z. Y.; Yin, Z. Y.; Sim, D. H.; Xiao, N.; Lim, T. M.; Hng, H. H.; Zhang, H.; Yan, Q. Y. Oriented Molecular Attachments through Sol-Gel Chemistry for Synthesis of Ultrathin Hydrated Vanadium Pentoxide Nanosheets and Their Applications. *Small* **2013**, *9*, 716–721.
5. Xu, C.; Zeng, Y.; Rui, X. H.; Xiao, N.; Zhu, J. X.; Zhang, W. Y.; Chen, J.; Liu, W. L.; Tan, H. T.; Hng, H. H.; *et al*. Controlled Soft-Template Synthesis of Ultrathin C@FeS Nanosheets with High-Li-Storage Performance. *ACS Nano* **2012**, *6*, 4713–4721.
6. Yang, S. B.; Feng, X. L.; Mullen, K. Sandwich-like, Graphene-Based Titania Nanosheets with High Surface Area for Fast Lithium Storage. *Adv. Mater.* **2011**, *23*, 3575–3579.
7. Novoselov, K. S.; Geim, A. K.; Morozov, S. V.; Jiang, D.; Zhang, Y.; Dubonos, S. V.; Grigorieva, I. V.; Firsov, A. A. Electric Field Effect in Atomically Thin Carbon Films. *Science* **2004**, *306*, 666–669.
8. Park, S.; Ruoff, R. S. Chemical Methods for the Production of Graphenes. *Nat. Nanotechnol.* **2009**, *4*, 217–224.
9. Zhu, Y. W.; Murali, S.; Cai, W. W.; Li, X. S.; Suk, J. W.; Potts, J. R.; Ruoff, R. S. Graphene and Graphene Oxide: Synthesis, Properties, and Applications. *Adv. Mater.* **2010**, *22*, 3906–3924.
10. Guo, H. L.; Wang, X. F.; Qian, Q. Y.; Wang, F. B.; Xia, X. H. A Green Approach to the Synthesis of Graphene Nanosheets. *ACS Nano* **2009**, *3*, 2653–2659.
11. Yu, T.; Lim, B.; Xia, Y. N. Aqueous-Phase Synthesis of Single-Crystal Ceria Nanosheets. *Angew. Chem., Int. Ed.* **2010**, *49*, 4484–4487.
12. Zhou, G. M.; Wang, D. W.; Yin, L. C.; Li, N.; Li, F.; Cheng, H. M. Oxygen Bridges between NiO Nanosheets and Graphene for Improvement of Lithium Storage. *ACS Nano* **2012**, *6*, 3214–3223.
13. Zhu, J. X.; Yin, Z. Y.; Li, H.; Tan, H. T.; Chow, C. L.; Zhang, H.; Hng, H. H.; Ma, J.; Yan, Q. Y. Bottom-Up Preparation of Porous Metal-Oxide Ultrathin Sheets with Adjustable Composition/Phases and Their Applications. *Small* **2011**, *7*, 3458–3464.
14. Ma, R. Z.; Sasaki, T. Nanosheets of Oxides and Hydroxides: Ultimate 2D Charge-Bearing Functional Crystallites. *Adv. Mater.* **2010**, *22*, 5082–5104.
15. Feng, J.; Peng, L. L.; Wu, C. Z.; Sun, X.; Hu, S. L.; Lin, C. W.; Dai, J.; Yang, J. L.; Xie, Y. Giant Moisture Responsiveness of $VS_2$ Ultrathin Nanosheets for Novel Touchless Positioning Interface. *Adv. Mater.* **2012**, *24*, 1969–1974.
16. Cunningham, G.; Lotya, M.; Cucinotta, C. S.; Sanvito, S.; Bergin, S. D.; Menzel, R.; Shaffer, M. S. P.; Coleman, J. N. Solvent Exfoliation of Transition Metal Dichalcogenides: Dispersibility of Exfoliated Nanosheets Varies only Weakly between Compounds. *ACS Nano* **2012**, *6*, 3468–3480.
17. Liu, H.; Su, D. W.; Zhou, R. F.; Sun, B.; Wang, G. X.; Qiao, S. Z. Highly Ordered Mesoporous $MoS_2$ with Expanded Spacing of the (002) Crystal Plane for Ultrafast Lithium Ion Storage. *Adv. Energy Mater.* **2012**, *2*, 970–975.
18. Chung, S. Y.; Bloking, J. T.; Chiang, Y. M. Electronically Conductive Phospho-olivines as Lithium Storage Electrodes. *Nat. Mater.* **2002**, *1*, 123–128.
19. Padhi, A. K.; Nanjundaswamy, K. S.; Goodenough, J. B. Phospho-olivines as Positive-Electrode Materials for Rechargeable Lithium Batteries. *J. Electrochem. Soc.* **1997**, *144*, 1188–1194.
20. Kang, B.; Ceder, G. Battery Materials for Ultrafast Charging and Discharging. *Nature* **2009**, *458*, 190–193.
21. Oh, S. W.; Myung, S. T.; Oh, S. M.; Oh, K. H.; Amine, K.; Scrosati, B.; Sun, Y. K. Double Carbon Coating of $LiFePO_4$ as High Rate Electrode for Rechargeable Lithium Batteries. *Adv. Mater.* **2010**, *22*, 4842–4845.
22. Wang, Y. G.; Wang, Y. R.; Hosono, E. J.; Wang, K. X.; Zhou, H. S. The Design of a $LiFePO_4$/Carbon Nanocomposite with a Core–Shell Structure and Its Synthesis by an *in Situ* Polymerization Restriction Method. *Angew. Chem., Int. Ed.* **2008**, *47*, 7461–7465.
23. Yoo, H.; Jo, M.; Jin, B. S.; Kim, H. S.; Cho, J. Flexible Morphology Design of 3D-Macroporous $LiMnPO_4$ Cathode Materials for Li Secondary Batteries: Ball to Flake. *Adv. Energy Mater.* **2011**, *1*, 347–351.
24. Wang, Y. G.; He, P.; Zhou, H. S. Olivine $LiFePO_4$: Development and Future. *Energy Environ. Sci.* **2011**, *4*, 805–817.
25. Devaraju, M. K.; Honma, I. Hydrothermal and Solvothermal Process Towards Development of $LiMPO_4$ (M = Fe, Mn) Nanomaterials for Lithium-Ion Batteries. *Adv. Energy Mater.* **2012**, *2*, 284–297.
26. Gwon, H.; Seo, D. H.; Kim, S. W.; Kim, J.; Kang, K. Combined First-Principle Calculations and Experimental Study on Multi-component Olivine Cathode for Lithium Rechargeable Batteries. *Adv. Funct. Mater.* **2009**, *19*, 3285–3292.
27. Herle, P. S.; Ellis, B.; Coombs, N.; Nazar, L. F. Nano-Network Electronic Conduction in Iron and Nickel Olivine Phosphates. *Nat. Mater.* **2004**, *3*, 147–152.
28. Fisher, C. A. J.; Prieto, V. M. H.; Islam, M. S. Lithium Battery Materials $LiMPO_4$ (M = Mn, Fe, Co, and Ni): Insights into Defect Association, Transport Mechanisms, and Doping Behavior. *Chem. Mater.* **2008**, *20*, 5907–5915.
29. Meethong, N.; Kao, Y. H.; Speakman, S. A.; Chiang, Y. M. Aliovalent Substitutions in Olivine Lithium Iron Phosphate and Impact on Structure and Properties. *Adv. Funct. Mater.* **2009**, *19*, 1060–1070.
30. Wang, G. X.; Liu, H.; Liu, J.; Qiao, S. Z.; Lu, G. Q. M.; Munroe, P.; Ahn, H. Mesoporous $LiFePO_4$/C Nanocomposite Cathode Materials for High Power Lithium Ion Batteries with Superior Performance. *Adv. Mater.* **2010**, *22*, 4944–4948.
31. Wu, X. L.; Jiang, L. Y.; Cao, F. F.; Guo, Y. G.; Wan, L. J. $LiFePO_4$ Nanoparticles Embedded in a Nanoporous Carbon Matrix: Superior Cathode Material for Electrochemical Energy-Storage Devices. *Adv. Mater.* **2009**, *21*, 2710–2714.
32. Oh, S. M.; Oh, S. W.; Yoon, C. S.; Scrosati, B.; Amine, K.; Sun, Y. K. High-Performance Carbon-$LiMnPO_4$ Nanocomposite Cathode for Lithium Batteries. *Adv. Funct. Mater.* **2010**, *20*, 3260–3265.
33. Xie, H. M.; Wang, R. S.; Ying, J. R.; Zhang, L. Y.; Jalbout, A. F.; Yu, H. Y.; Yang, G. L.; Pan, X. M.; Su, Z. M. Optimized $LiFePO_4$-Polyacene Cathode Material for Lithium-Ion Batteries. *Adv. Mater.* **2006**, *18*, 2609–2613.
34. Lu, Z. G.; Cheng, H.; Lo, M. F.; Chung, C. Y. Pulsed Laser Deposition and Electrochemical Characterization of $LiFePO_4$-Ag Composite Thin Films. *Adv. Funct. Mater.* **2007**, *17*, 3885–3896.
35. Hu, Y. S.; Guo, Y. G.; Dominko, R.; Gaberscek, M.; Jamnik, J.; Maier, J. Improved Electrode Performance of Porous $LiFePO_4$ Using $RuO_2$ as an Oxidic Nanoscale Interconnect. *Adv. Mater.* **2007**, *19*, 1963–1966.
36. Zhu, C. B.; Yu, Y.; Gu, L.; Weichert, K.; Maier, J. Electrospinning of Highly Electroactive Carbon-Coated Single-Crystalline $LiFePO_4$ Nanowires. *Angew. Chem., Int. Ed.* **2011**, *50*, 6278–6282.
37. Lee, M. H.; Kim, J. Y.; Song, H. K. A Hollow Sphere Secondary Structure of $LiFePO_4$ Nanoparticles. *Chem. Commun.* **2010**, *46*, 6795–6797.
38. Nishimura, S.; Kobayashi, G.; Ohoyama, K.; Kanno, R.; Yashima, M.; Yamada, A. Experimental Visualization of Lithium Diffusion in $Li_xFePO_4$. *Nat. Mater.* **2008**, *7*, 707–711.
39. Yuan, A. Q.; Wu, J.; Bai, L. J.; Ma, S. M.; Huang, Z. Y.; Tong, Z. F. Standard Molar Enthalpies of Formation for Ammonium/3d-Transition Metal Phosphates $NH_4MPO_4$ Center Dot $H_2O$ (M = $Mn^{2+}$, $Co^{2+}$, $Ni^{2+}$, $Cu^{2+}$). *Chem. Eng. Data* **2008**, *53*, 1066–1070.
40. Wang, L.; He, X. M.; Sun, W. T.; Wang, J. L.; Li, Y. D.; Fan, S. S. Crystal Orientation Tuning of $LiFePO_4$ Nanoplates for High Rate Lithium Battery Cathode Materials. *Nano Lett.* **2012**, *12*, 5632–5636.

41. Rui, X. H.; Sim, D. H.; Xu, C.; Liu, W. L.; Tan, H. T.; Wong, K. M.; Hng, H. H.; Lim, T. M.; Yan, Q. Y. One-Pot Synthesis of Carbon-Coated $VO_2$(B) Nanobelts for High-Rate Lithium Storage. *RSC Adv.* **2012**, *2*, 1174–1180.
42. Wolfenstine, J.; Allen, J. $Ni^{3+}/Ni^{2+}$ Redox Potential in $LiNiPO_4$. *J. Power Sources* **2005**, *142*, 389–390.
43. Delacourt, C.; Laffont, L.; Bouchet, R.; Wurm, C.; Leriche, J. B.; Morcrette, M.; Tarascon, J. M.; Masquelier, C. Toward Understanding of Electrical Limitations (Electronic, Ionic) in $LiMPO_4$ (M = Fe, Mn) Electrode Materials. *J. Electrochem. Soc.* **2005**, *152*, A913–A921.
44. Arico, A. S.; Bruce, P.; Scrosati, B.; Tarascon, J. M.; Van Schalkwijk, W. Nanostructured Materials for Advanced Energy Conversion and Storage Devices. *Nat. Mater.* **2005**, *4*, 366–377.
45. Wang, G. P.; Zhang, L.; Zhang, J. J. A Review of Electrode Materials for Electrochemical Supercapacitors. *Chem. Soc. Rev.* **2012**, *41*, 797–828.
46. Kovalenko, I.; Zdyrko, B.; Magasinski, A.; Hertzberg, B.; Milicev, Z.; Burtovyy, R.; Luzinov, I.; Yushin, G. A Major Constituent of Brown Algae for Use in High-Capacity Li-Ion Batteries. *Science* **2011**, *333*, 75–79.
47. Brezesinski, T.; Wang, J.; Tolbert, S. H.; Dunn, B. Ordered Mesoporous α-$MoO_3$ with Iso-Oriented Nanocrystalline Walls for Thin-Film Pseudocapacitors. *Nat. Mater.* **2010**, *9*, 146–151.
48. Zhang, X. J.; Shi, W. H.; Zhu, J. X.; Kharistal, D. J.; Zhao, W. Y.; Lalia, B. S.; Hng, H. H.; Yan, Q. Y. High-Power and High-Energy-Density Flexible Pseudocapacitor Electrodes Made from Porous CuO Nanobelts and Single-Walled Carbon Nanotubes. *ACS Nano* **2011**, *5*, 2013–2019.
49. Zhou, S.; Yang, X. G.; Lin, Y. J.; Xie, J.; Wang, D. W. A Nanonet-Enabled Li Ion Battery Cathode Material with High Power Rate, High Capacity, and Long Cycle Lifetime. *ACS Nano* **2012**, *6*, 919–924.
50. Zhu, J. X.; Yin, Z. Y.; Yang, D.; Sun, T.; Yu, H.; Hoster, H. E.; Hng, H. H.; Zhang, H.; Yan, Q. Y. Hierarchical Hollow Spheres Composed of Ultrathin $Fe_2O_3$ Nanosheets for Lithium Storage and Photocatalytic Water Oxidation. *Energy Environ. Sci.* **2013**, *6*, 987–993.
51. Rangappa, D.; Murukanahally, K. D.; Tomai, T.; Unemoto, A.; Honma, I. Ultrathin Nanosheets of $Li_2MSiO_4$ (M = Fe, Mn) as High-Capacity Li-Ion Battery Electrode. *Nano Lett.* **2012**, *12*, 1146–1151.
52. Wu, Z. S.; Ren, W. C.; Xu, L.; Li, F.; Cheng, H. M. Doped Graphene Sheets As Anode Materials with Superhigh Rate and Large Capacity for Lithium Ion Batteries. *ACS Nano* **2011**, *5*, 5463–5471.
53. Morgan, D.; Van der Ven, A.; Ceder, G. Li Conductivity in $Li_xMPO_4$ (M = Mn, Fe, Co, Ni) Olivine Materials. *Electrochem. Solid State Lett.* **2004**, *7*, A30–A32.
54. Rui, X. H.; Jin, Y.; Feng, X. Y.; Zhang, L. C.; Chen, C. H. A Comparative Study on the Low-Temperature Performance of $LiFePO_4$/C and $Li_3V_2(PO_4)_3$/C Cathodes for Lithium-Ion Batteries. *J. Power Sources* **2011**, *196*, 2109–2114.